

Sheet-on-sheet architectural assembly of MOF/graphene for high-stability NO sensing at room temperature

Chang, Yanwei; Zhang, Jingxing; Lu, Ruofei; Li, Weiran; Feng, Yuchen; Gao, Yixun; Yang, Haihong; Wang, Fengnan; French, Patrick J.; More Authors

DOI

[10.1039/d4tc00091a](https://doi.org/10.1039/d4tc00091a)

Publication date

2024

Document Version

Final published version

Published in

Journal of Materials Chemistry C

Citation (APA)

Chang, Y., Zhang, J., Lu, R., Li, W., Feng, Y., Gao, Y., Yang, H., Wang, F., French, P. J., & More Authors (2024). Sheet-on-sheet architectural assembly of MOF/graphene for high-stability NO sensing at room temperature. *Journal of Materials Chemistry C*, 12(21), 7520-7531. <https://doi.org/10.1039/d4tc00091a>

Important note

To cite this publication, please use the final published version (if applicable).
Please check the document version above.

Copyright

Other than for strictly personal use, it is not permitted to download, forward or distribute the text or part of it, without the consent of the author(s) and/or copyright holder(s), unless the work is under an open content license such as Creative Commons.

Takedown policy

Please contact us and provide details if you believe this document breaches copyrights.
We will remove access to the work immediately and investigate your claim.

Green Open Access added to TU Delft Institutional Repository

'You share, we take care!' - Taverne project

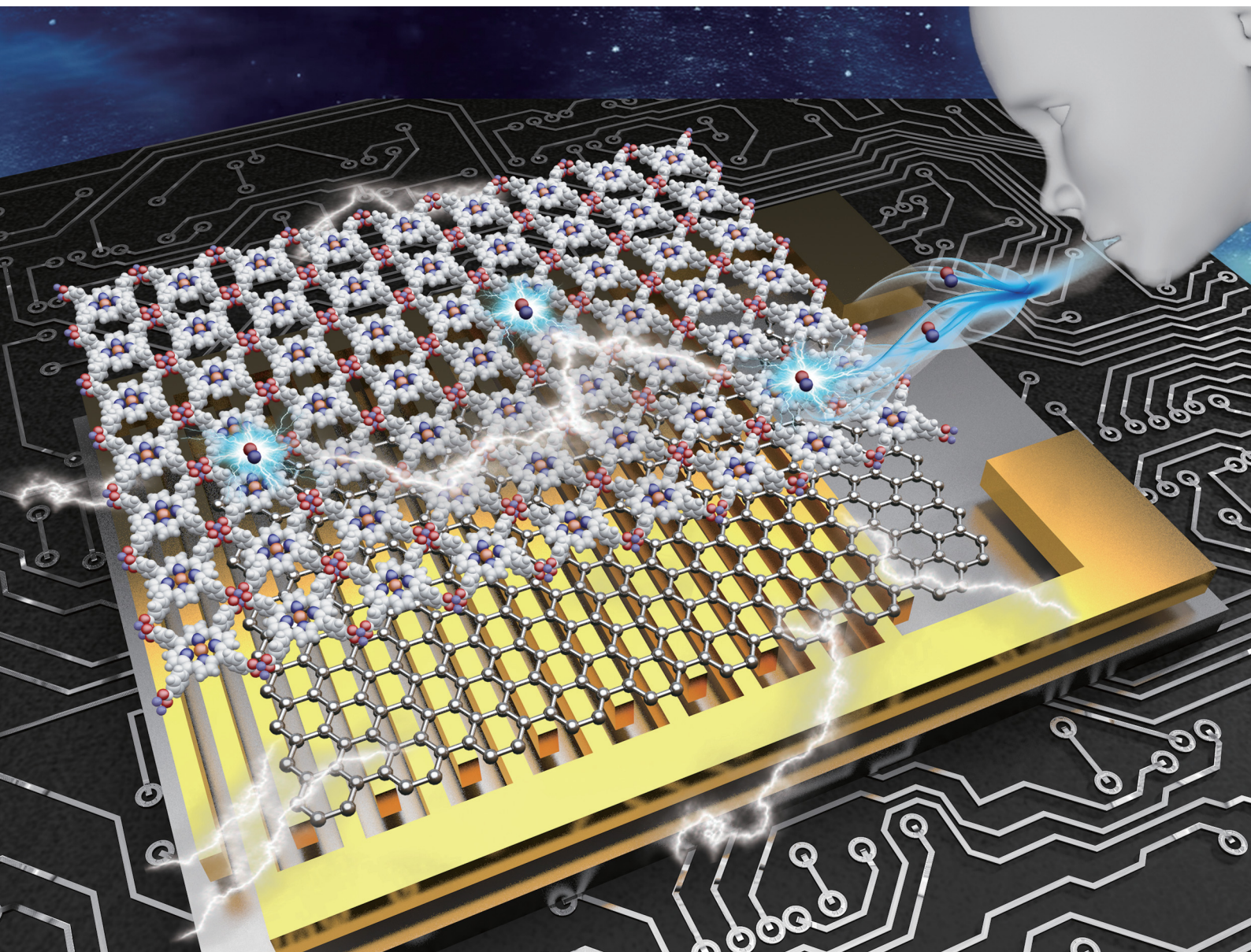
<https://www.openaccess.nl/en/you-share-we-take-care>

Otherwise as indicated in the copyright section: the publisher is the copyright holder of this work and the author uses the Dutch legislation to make this work public.

Journal of Materials Chemistry C

Materials for optical, magnetic and electronic devices

rsc.li/materials-c



ISSN 2050-7526

Cite this: *J. Mater. Chem. C*,
2024, 12, 7520

Sheet-on-sheet architectural assembly of MOF/graphene for high-stability NO sensing at room temperature†

Yanwei Chang,^{ab} Jingxing Zhang,^{ab} Ruofei Lu,^{ab} Weiran Li,^{ab} Yuchen Feng,^c Yixun Gao,^{ab} Haihong Yang,^d Fengnan Wang,^d Hao Li,^{ab} Yi-Kuen Lee,^{ef} Patrick J. French,^g Ahmad M. Umar Siddiqui,^h Yao Wang,^{ab} and Guofu Zhou^{ab}

Fractional exhaled nitric oxide (FeNO) can be used to describe inflammatory processes in the respiratory tract. Directly detecting ppb-level nitric oxide (NO) with chemiresistive sensors at room temperature faces the challenges of simultaneously obtaining high sensitivity and high stability for sensors. We aimed to improve the stability and sensitivity of NO sensors. We assembled sheet-like porphyrin-based MOF DLS-2D-Co-TCPP(Fe) with 5-aminonaphthalene-1-sulfonic acid-rGO (ANS-rGO) nanosheets through coordination interactions. In this way, we offered a room-temperature NO-sensing hybrid, DLS-2D-Co-TCPP(Fe)/ANS-rGO, with a sheet-on-sheet (SOS) architectural heterojunction. The DLS-2D-Co-TCPP(Fe)/ANS-rGO-based sensor demonstrated superior NO-sensing performance, including high sensitivity ($R_a/R_g = 1.33$, 250 ppb), reliable repeatability, high selectivity, and fast response/recovery (150 s/185 s, 1 ppm) at a sensing concentration from 100 ppb to 10 ppm at room temperature. The obtained sensor showed high stability, retaining >85% of its initial response after 60 days. Designing NO-responsive Fe-N₄ active units containing MOF nanosheets, along with constructing a heterojunction with an SOS architecture to facilitate carrier migration, collaboratively dominated the superior performance of synthesized NO sensors. This work provides a strategy for designing SOS architectural heterojunctions to obtain high-performance MOF-based gas-sensing materials.

Received 8th January 2024,
Accepted 9th April 2024

DOI: 10.1039/d4tc00091a

rsc.li/materials-c

^a Guangdong Provincial Key Laboratory of Optical Information Materials and Technology, Institute of Electronic Paper Displays, South China Academy of Advanced Optoelectronics, South China Normal University, Guangzhou 510006, P. R. China. E-mail: wangyao@m.scnu.edu.cn

^b National Center for International Research on Green Optoelectronics, South China Normal University, Guangzhou 510006, P. R. China

^c Fujian Agriculture and Forestry University, School of Future Technology, China

^d Department of Thoracic Oncology, State Key Laboratory of Respiratory Diseases, The First Affiliated Hospital of Guangzhou Medical University, Guangzhou, 510006, P. R. China

^e Department of Mechanical & Aerospace Engineering, Hong Kong University of Science and Technology, Clear Water Bay, Kowloon, Hong Kong SAR

^f Department of Electronic & Computer Engineering, Hong Kong University of Science and Technology, Clear Water Bay, Kowloon, Hong Kong SAR

^g BE Laboratory, EWI, Delft University of Technology, Delft 2628CD, The Netherlands

^h Department of Chemistry, Faculty of Science and Arts and Promising Centre for Sensors and Electronic Devices (PCSED), Najran University, Najran, 11001, Saudi Arabia

† Electronic supplementary information (ESI) available: Section 1: FTIR spectra. Section 2: XRD patterns. Section 3: BET analysis. Section 4: XPS spectra. Section 5: humidity response test. Section 6: preparation of gas samples. Section 7: gas response test. Section 8: gas-sensing measurements. Section 9: structural characterization. Section 10: synthesis of TCPP(Fe). Section 11: synthesis of Co-TCPP(Fe)-Rod MOF. Section 12: Synthesis of ANS-rGO. Section 13: Synthesis of Co-TCPP(Fe)-Rod/ANS-rGO. See DOI: <https://doi.org/10.1039/d4tc00091a>

Introduction

Nitric oxide (NO) is an important biological signaling molecule produced endogenously by the human-body metabolism.^{1,2} Fractional exhaled nitric oxide (FeNO) <100 ppb denotes airway inflammation, which could be adopted to predict treatment effects against asthma and evaluate respiratory diseases.³ Therefore, detecting ppb-level NO is important in the clinical diagnosis of respiratory diseases. Chemiresistive gas sensors based on the change in the resistance signal are widely used NO sensors owing to their small size, high sensitivity, low cost, and convenient operation.^{4–6} Metal oxide semiconductors (MOSS) are the primary sensing materials for ppb-level NO in chemiresistive gas sensors because of their high sensitivity. However, the gas-sensing processes of MOSS require the essential active units of oxygen species which generate only under high temperature (generally 100–400 °C) and exhibit unsatisfactory selectivity.^{7–15} Therefore, how to achieve high selectivity of NO sensing at room temperature is the first key issue to realize its practicability.^{16–18}

Fortunately, two-dimensional metal-organic frameworks (2D MOFs) exhibit great potential for realizing high-selectivity

chemiresistive NO sensing because NO can be selectively chemisorbed by specific metal- N_4 ($M-N_4$) active units within 2D MOFs at room temperature.^{19–21} Mirica *et al.* adopted the organic ligand 2,3,5,6,10,11-hexahydroxytriphenylene (HHTP) and Ni(II) to obtain Ni- N_4 active units-containing 2D MOF (Ni_3HHTP_2). The Ni_3HHTP_2 -based chemiresistive sensor showed high selectivity for NO sensing at room temperature, but the ppm-level practical limit of detection (pLOD) of the sensor made it unsuitable for practical application, which resulted from the limited carrier concentration within 2D MOFs.^{22–26}

Using 2D MOFs-based sensors to reach high-selectivity ppb-level NO sensing at room temperature is a rational approach. Without concern about 2D MOF lattice matching issue, an approach of combining 2D MOFs with 2D conductive materials to construct heterojunctions through supramolecular self-assembly has been developed to improve the carrier concentration and carrier migration within 2D MOFs.^{27–29} For example, in 2023, Wang *et al.* used this strategy for high-selectivity ppb-level NO sensing at room temperature to design porphyrin-based rod-like 2D MOFs to build a MOF/MXene hybrid-based NO sensor. The latter showed superior sensing properties toward NO at room temperature because 2D MOFs provided an effective platform for Fe- N_4 active units to selectively chemisorb NO, though the long-term stability of the sensor was 10 days.^{30–32} Compared with MXene, graphene, as a more stable 2D conductive material, has been considered to be a distinctive and efficient functional scaffold with 2D MOFs to fabricate heterojunctions.^{33,34} In 2023, Wu *et al.* prepared a NO sensor with Co- N_4 active units, which assembled by rod-like 2D MOFs of $Co_3(HITP)_2$ (HITP, 2,3,6,7,10,11-hexaiminotriphenylene) with reduced graphene oxide (rGO), to achieve an outstanding NO performance with a sensing range of 0.1–1 ppm, though the sensing response declined 60% of the initial value after only 12 days.³⁵ This inadequate stability could be due to two reasons. On the one hand, MOFs with rod-like morphology possess limited contact area with 2D conductive materials, which cannot provide enough interaction to form stable heterojunctions. On the other hand, rGO possesses high specific surface energy and naturally tends to self-aggregate, which also limits the formation of heterojunctions.^{36,37}

The second key issue for a gas sensor for practical application is high stability. Sheet-on-sheet (SOS) architectural heterojunctions provide larger contact area between 2D MOF nanosheets and graphene nanosheets, which is beneficial for forming stable heterojunctions with high carrier concentration and high carrier migration to sense NO at room temperature. Therefore, 2D MOFs and graphene with high dispersion, large size, and sheet-like morphology are ideal to construct SOS architectural heterojunctions.

“Bottom-up” and “top-down” are typical approaches for preparing 2D MOFs with a well dispersed, large-size, and sheet-like morphology. Herein, we defined 2D MOFs with high dispersion, large size, and sheet-like morphology as “DLS-2D MOFs”. Surfactant (*e.g.*, polyvinylpyrrolidone (PVP))-assisted synthesis shows an effective bottom-up way to obtain DLS-2D MOFs because PVP can selectively attach on the surface of 2D

MOFs, leading to the anisotropic growth of MOFs and formation of 2D MOF nanosheets.³⁸ Unfortunately, the presence of PVP on the surface of DLS-2D MOFs would negatively affect the exposure of active sites but also carrier migration.³⁹ In contrast, the top-down approach of using liquid-phase exfoliation to avoid the introduction of a polymer on the surface of MOFs could be a better choice to prepare DLS-2D MOF nanosheets with a clean surface and more exposible active sites.⁴⁰ With regard to the preparation of high-quality rGO with high dispersion, large size and sheet-like morphology (we defined rGO with high dispersion, large size, and sheet-like morphology as “DLS-rGO”), a self-assembling strategy developed in our previous work would work.⁴¹ Thus, we had all the strategies to construct a SOS architectural heterojunction of DLS-2D MOF/DLS-rGO.

In this work, a DLS-2D-Co-TCPP(Fe)/ANS-rGO architectural heterojunction was prepared through coordination interaction between DLS-2D-Co-TCPP(Fe) and ANS-rGO. As expected, the obtained NO sensors exhibited superior sensing performance towards NO at room temperature, including a pLOD of 100 ppb, excellent selectivity, and long-term stability. Study of the gas-sensing mechanism demonstrated that designing NO-responsive Fe- N_4 active units containing MOF nanosheets, along with constructing a SOS architectural heterojunction of MOF/graphene nanosheets, jointly dominated the superior performance of the obtained DLS-2D-Co-TCPP(Fe)/ANS-rGO-based NO sensor.

Experimental section

Materials

Tetrakis (4-carboxyphenyl) porphyrin (TCPP, 97%) was purchased from Alf. Cobalt nitrate hexahydrate ($Co(NO_3)_2 \cdot 6H_2O$, 98%) was obtained from Innochem. *N,N*-Dimethylformamide (DMF, 99.8%) was purchased from Aladdin. Ethanol was sourced from Acros. All materials were used as received without further purification. The synthesis of TCPP(Fe), Co-TCPP(Fe)-Rod MOF, and ANS-rGO are described in ESI.†

Synthesis of DLS-2D-Co-TCPP(Fe) MOF

First, we fabricated DLS-2D-Co-TCPP(Fe). Briefly, an ethanol suspension of Co-TCPP(Fe)-Rod (10 mg/6 mL) in a 10-mL vial was sonicated for 40 min at 60 Hz at 50 °C and then filtered. Finally, the obtained DLS-2D-Co-TCPP(Fe) MOF nanosheets were redispersed in 5 mL of ethanol.

Synthesis of a DLS-2D-Co-TCPP(Fe)/ANS-rGO SOS architectural heterojunction

First, we fabricated DLS-2D-Co-TCPP(Fe)/ANS-rGO. Briefly, DLS-2D-Co-TCPP(Fe)/ANS-rGO hybrid was prepared through supramolecular self-assembly. Then, a certain volume of an ethanol suspension of DLS-2D-Co-TCPP(Fe) and deionized water suspension of ANS-rGO was added to a 20-ml capped vial. After that, the suspension was sonicated at 60 Hz for 20 min at 50 °C. The obtained products were allowed to stand

under a vacuum at 40 °C for 60 min. Finally, the hybrids were kept under nitrogen. DLS-2D-Co-TCPP(Fe)/ANS-rGO hybrids with different feed mass ratios from 0.05 : 1 to 0.9 : 1 (DLS-2D-Co-TCPP(Fe):ANS-rGO, m:m) were prepared by controlling the feed mass ratio, and were named DLS-2D-Co-TCPP(Fe)/ANS-rGO-0.05, DLS-2D-Co-TCPP(Fe)/ANS-rGO-0.1, DLS-2D-Co-TCPP(Fe)/ANS-rGO-0.3, DLS-2D-Co-TCPP(Fe)/ANS-rGO-0.5, and DLS-2D-Co-TCPP(Fe)/ANS-rGO-0.9, respectively.

Gas sensing

Gas sensors were fabricated using the drop-dry method, wherein 10 μL of a dispersion of a well-dispersed gas-sensing material (10 mg mL^{-1}) was uniformly applied onto the interdigital electrodes (IDEs) of a ceramic substrate. Subsequently, the sensors were dried at 50 °C on a heating holder for 5 min to facilitate the preparation of gas sensors for subsequent gas-sensitive testing. The alterations in sensor resistance were tracked using an electrometer (2450 series; Keithley).

The reaction of a target gas with a sensing material causes a change in sensor resistance. Hence, the changes in current shown on the electrometer can be observed before and after injection of the target gas under an excitation voltage of 0.1 VDC. In this work, gas-sensing tests of all materials were performed at room temperature (25 ± 2 °C) in a background of dry N_2 .

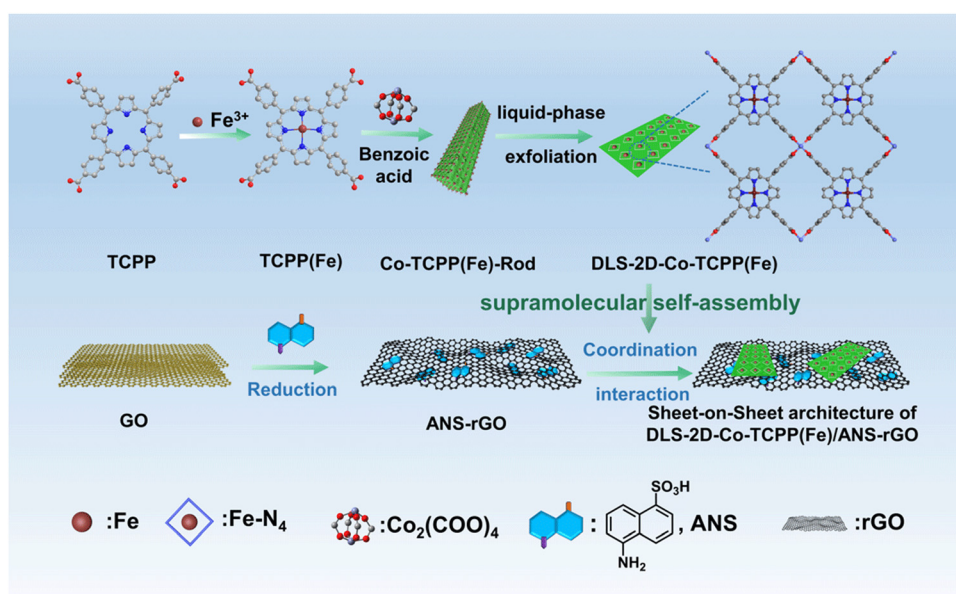
Typically, the response (S) to gas is represented as R_a/R_g , where R_a and R_g denote the resistance of the gas sensor in nitrogen and target gases, respectively. In the present study, the response S to NO was specifically defined as R_a/R_g due to its pronounced oxidizing nature. Conventionally, the response/recovery time is characterized as the time taken to attain 90% response from the moment the gas sensor is exposed/removed from the gas. The pLOD is commonly defined as the minimal concentration of the target gas detectable by the gas sensor.

Results and discussion

The fabrication processes of TCPP(Fe), Co-TCPP(Fe)-Rod, DLS-2D-Co-TCPP(Fe), ANS-rGO, and DLS-2D-Co-TCPP(Fe)/ANS-rGO are demonstrated in Scheme 1.

Co-TCPP(Fe)-Rod was fabricated from TCPP(Fe) and Co^{2+} by a solvothermal reaction. DLS-2D-Co-TCPP(Fe) with high dispersion, large size, and sheet-like morphology was obtained from Co-TCPP(Fe)-Rod MOF by liquid-phase exfoliation. ANS-rGO was fabricated by ANS, GO, and hydrazine hydrate by a hydrothermal reduction method. DLS-2D-Co-TCPP(Fe)/ANS-rGO hybrid was prepared by assembling DLS-2D-Co-TCPP(Fe) with ANS-rGO *via* supramolecular self-assembly. Details of these syntheses are given in the Experimental section. The morphologies of the synthesized Co-TCPP(Fe)-Rod, DLS-2D-Co-TCPP(Fe), and DLS-2D-Co-TCPP(Fe)/ANS-rGO-0.5 (*i.e.*, the feed mass ratio of DLS-2D-Co-TCPP(Fe) to ANS-rGO was 0.5 : 1 in this composite) were revealed by scanning electron microscopy (SEM) and atomic force microscopy (AFM). Fig. 1(a) and (b) show that Co-TCPP(Fe)-Rod had a rod-like morphology, aggregating by rectangular nanosheets ($1\text{--}5 \mu\text{m} \times 0.2\text{--}1 \mu\text{m}$).

SEM images and AFM image in Fig. 1(c), (d), and (e) reveal DLS-2D-Co-TCPP(Fe) to have a sheet-like shape of length $1\text{--}4 \mu\text{m}$, width of $0.2\text{--}1 \mu\text{m}$, and thickness of 50 nm. Hence, DLS-2D-Co-TCPP(Fe) with high dispersion, large size, and sheet-like morphology was prepared by liquid-phase exfoliation. Fig. 1(e) and (f) show that DLS-2D-Co-TCPP(Fe) formed a composite with ANS-rGO uniformly, indicating that DLS-2D-Co-TCPP(Fe)/ANS-rGO hybrid had been obtained, which was the precondition for heterojunction formation. At this point, based on the SEM image of DLS-2D-Co-TCPP(Fe)/ANS-rGO-0.5 (Fig. 1(e) and (f)), X-ray diffraction (XRD) (Fig. S2, ESI[†]) and the feed mass ratio of assemblies, rGO/rGO/MOF/rGO was the main



Scheme 1 Fabrication process of Co-TCPP(Fe)-Rod, DLS-2D-Co-TCPP(Fe), ANS-rGO, and DLS-2D-Co-TCPP(Fe)/ANS-rGO.

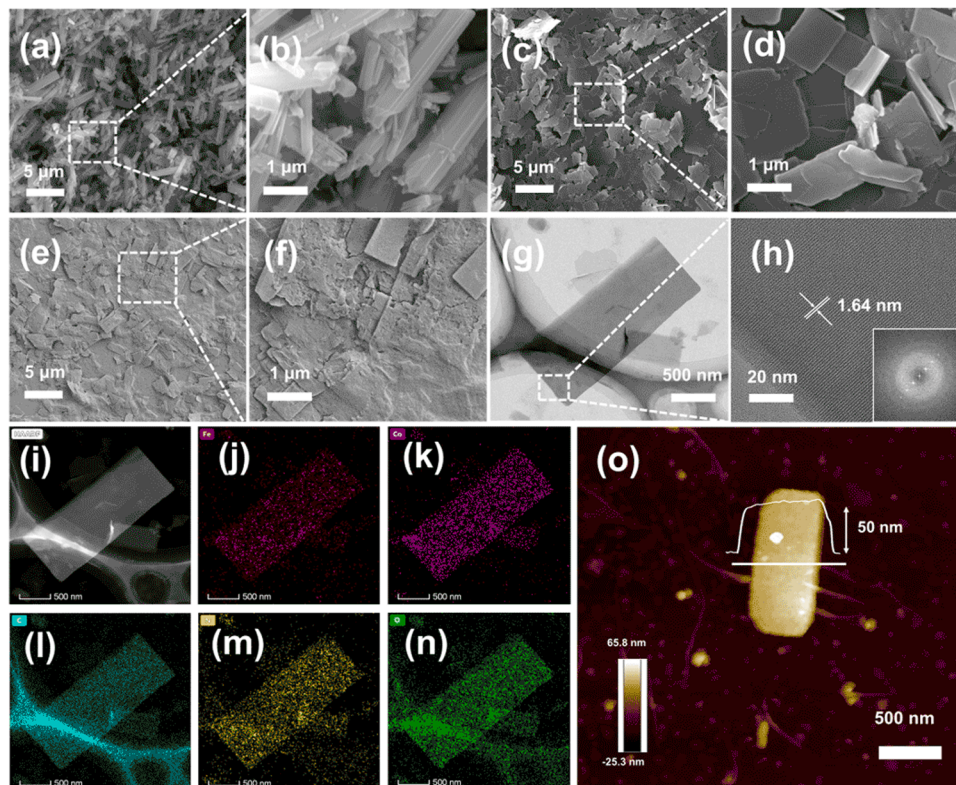


Fig. 1 SEM images of (a) and (b) Co-TCPP(Fe)-Rod, (c) and (d) DLS-2D-Co-TCPP(Fe), (e) and (f) DLS-2D-Co-TCPP(Fe)/ANS-rGO, where (b), (d), and (f) are at higher magnifications. TEM images of (g) and (h) DLS-2D-Co-TCPP(Fe), where (h) is at a higher magnification and corresponding FFT patterns (inset). HAADF-STEM images of (i) DLS-2D-Co-TCPP(Fe). TEM elemental mapping images of (j) Fe, (k) Co, (l) C, (m) N, and (n) O. (o) AFM image of DLS-2D-Co-TCPP(Fe).

SOS architecture in the final assembly because aggregation of the over-addition rGO nanosheets was inevitable.

For DLS-2D-Co-TCPP(Fe), the detailed morphology, as well as the composition and distribution of elements were demonstrated by transmission electron microscopy (TEM) and high-angle annular dark-field scanning transmission electron microscopy (HAADF-STEM). As shown in Fig. 1(g)–(i), DLS-2D-Co-TCPP(Fe) had obvious lattice fringes. The lattice was ~ 1.64 nm, which is accordant with reports.^{42,43} TEM elemental mapping images showed Fe, Co, C, N, and O to be distributed on DLS-2D-Co-TCPP(Fe) nanosheets homogeneously (Fig. 1(j)–(n)). Notably, Fe and N were uniformly distributed in the whole nanosheets of MOF (Fig. 1(j) and (m)), indicating that MOF had been fabricated.⁴²

Ultraviolet-visible absorption spectroscopy (UV-Vis) of TCPP and TCPP(Fe) displayed the central coordination of the porphyrin ligand. Generally, the Soret band on behalf of the transition to the second excited singlet state (S_2) was at 380–450 nm.⁴⁴ Meanwhile, the Q band was typically identified as the lowest excited singlet state (S_1) of the transition at about 500–750 nm.⁴⁵

In Fig. 2(a), TCPP showed B-band absorption at 415 nm, while TCPP(Fe) had significant Soret-band absorption at 423 nm. The significant red-shift indicated that iron ions entered the inner ring of porphyrin ligands.⁴⁶ In addition, after

TCPP was prepared into TCPP(Fe), the absorption peak of the Q band changed from 515 nm, 549 nm, 592 nm, and 646 nm to 562 nm, further indicating the chelate Fe^{3+} in the porphyrin ring with four N atoms.⁴⁷ The formation of $Fe-N_4$ active units was the key structure as active sites to sense NO.^{30,48–50}

XRD demonstrated the crystal structure of MOFs. As displayed in Fig. 2(b), the typical peaks of Co-TCPP(Fe)-Rod and DLS-2D-Co-TCPP(Fe) at (110), (101), and (200) in the XRD pattern demonstrated that $Co_2(COO)_4$ “paddlewheel” units had been formed.⁵¹ The poor crystallinity of the MOF could be related to the atomic defects induced by solvothermal synthesis and crystal-structure damage caused by liquid-phase exfoliation.^{52–58} The XRD patterns of different feed mass fractions of DLS-2D-Co-TCPP(Fe)/ANS-rGO are demonstrated in Fig. S2 (ESI[†]). The XRD data of DLS-2D-Co-TCPP(Fe)/ANS-rGO-0.5 and DLS-2D-Co-TCPP(Fe)/ANS-rGO-0.5 after 60 days were almost identical, and Co-TCPP(Fe) MOF contained two hybrids peaks. The XRD data of the obtained Co-TCPP(Fe)-Rod and DLS-2D-Co-TCPP(Fe) were consistent with the simulated standard diagram of Co-TCPP(Fe) MOF, demonstrating paddlewheel $Co_2(COO)_4$ metal nodes to be connected by tetracarboxylic TCPP(Fe) ligands to form an AB stacking mode with an interlayer spacing of 6.9 Å. (Fig. 2(c) and (d)).⁵⁹

Electrochemical impedance spectroscopy (EIS) was conducted to describe the electrical performance of Co-TCPP(Fe)-

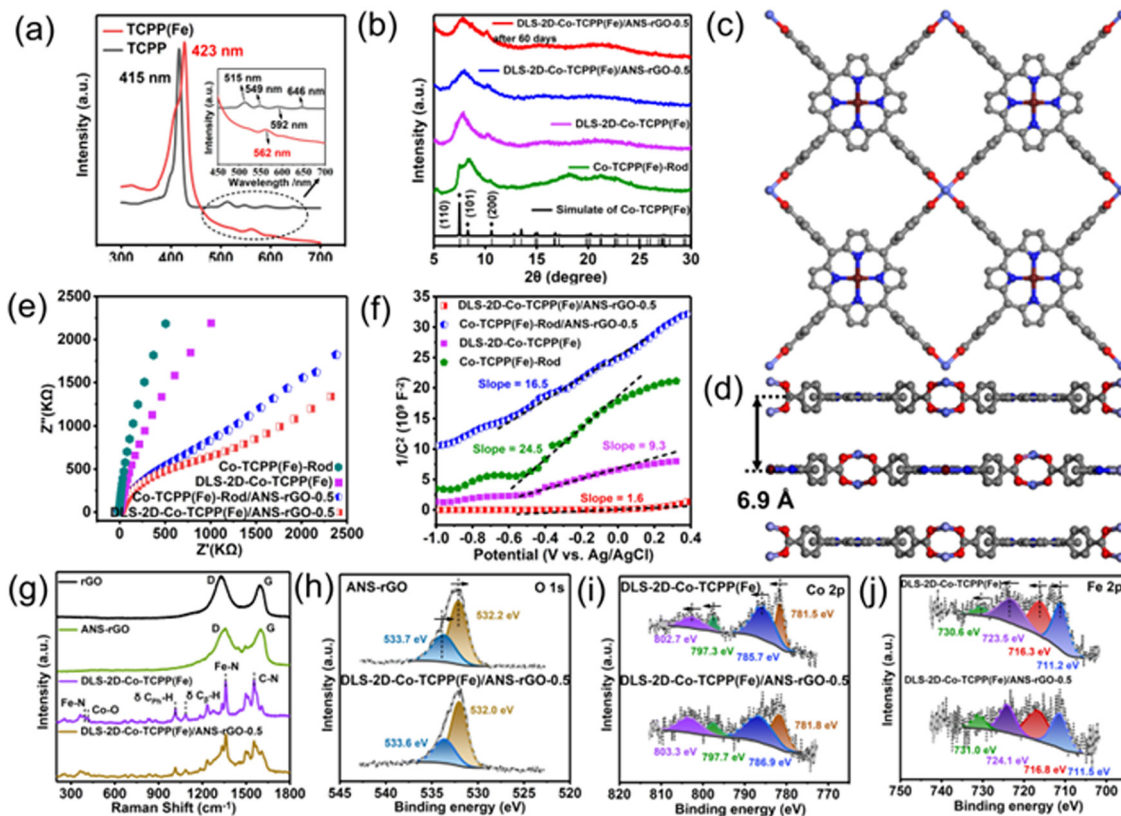


Fig. 2 (a) UV-Vis absorption spectra of TCPP and TCPP(Fe). (b) XRD of DLS-2D-Co-TCPP(Fe)/ANS-rGO-0.5 after 60 days, DLS-2D-Co-TCPP(Fe)/ANS-rGO-0.5, DLS-2D-Co-TCPP(Fe), Co-TCPP(Fe)-Rod, and simulated of Co-TCPP(Fe). (c) and (d) Constructed structural model for Co-TCPP(Fe)-Rod. (e) Nyquist plots of Co-TCPP(Fe)-Rod, DLS-2D-Co-TCPP(Fe), Co-TCPP(Fe)-Rod/ANS-rGO-0.5, and DLS-2D-Co-TCPP(Fe)/ANS-rGO-0.5. (f) Mott-Schottky plots of Co-TCPP(Fe)-Rod, DLS-2D-Co-TCPP(Fe), Co-TCPP(Fe)-Rod/ANS-rGO-0.5, and DLS-2D-Co-TCPP(Fe)/ANS-rGO-0.5 electrodes measured in 1 M Na₂SO₄ solution with a frequency of 100 Hz. (g) Raman spectra of rGO, ANS-rGO, DLS-2D-Co-TCPP(Fe), and DLS-2D-Co-TCPP(Fe)/ANS-rGO-0.5. High-resolution XPS spectra of (h) O 1s of ANS-rGO. High-resolution XPS spectra of (i) Co 2p, (j) Fe 2p of DLS-2D-Co-TCPP(Fe) and DLS-2D-Co-TCPP(Fe)/ANS-rGO-0.5.

Rod and DLS-2D-Co-TCPP(Fe). Generally, Nyquist plots described the carrier migration resistance (R_{ct}) and electron-transfer properties between Co-TCPP(Fe)/electrolyte interfaces by the diameter of a semicircle. The smaller the diameter of a semicircle in Nyquist plots, the lower is the R_{ct} .⁶⁰ As shown in Fig. 2(e), the simulated R_{ct} values of Co-TCPP(Fe)-Rod were larger than those of DLS-2D-Co-TCPP(Fe), indicating that DLS-2D-Co-TCPP(Fe) possessed higher electrical conductivity than that of Co-TCPP(Fe)-Rod because DLS-2D-Co-TCPP(Fe) possessed lower resistance than that of Co-TCPP(Fe)-Rod. Meanwhile, after assembly with ANS-rGO, the obtained R_{ct} values of Co-TCPP(Fe)-Rod/ANS-rGO and DLS-2D-Co-TCPP(Fe)/ANS-rGO were decreased, indicating that ANS-rGO could improve the carrier migration and carrier concentration of the hybrid. As displayed in Fig. 2(f), the Mott-Schottky plots of Co-TCPP(Fe)-Rod and DLS-2D-Co-TCPP(Fe) were characterized by positive slopes, indicating that both MOFs were n-type semiconductors.⁶¹ In addition, the smaller slope of DLS-2D-Co-TCPP(Fe) compared with that of Co-TCPP(Fe)-Rod signified a greater carrier concentration in DLS-2D-Co-TCPP(Fe), which aligned with the characterization results of EIS. Thus, the lower resistance of DLS-2D-Co-TCPP(Fe) than Co-TCPP(Fe)-Rod could result in a response enhancement for NO sensing. Furthermore,

DLS-2D-Co-TCPP(Fe)/ANS-rGO had better carrier migration and carrier concentration, which was provided by ANS-rGO, and facilitated the sensitivity of NO sensing. Fourier transform infrared (FTIR) spectroscopy was employed to analyze rGO, ANS-rGO, TCPP, TCPP(Fe), Co-TCPP(Fe)-Rod, DLS-2D-Co-TCPP(Fe), Co-TCPP(Fe)-Rod/ANS-rGO, and DLS-2D-Co-TCPP(Fe)/ANS-rGO (Fig. S1, ESI[†]). For rGO and ANS-rGO, a vibration due to the C=C skeleton appeared at 1628 cm⁻¹. The characteristic peaks of S=O stretching bands at 1196–1032 cm⁻¹ and a peak representing naphthyl-ring absorption at 1576 cm⁻¹ indicated that rGO was assembled with ANS.⁴¹ For TCPP, a band at 964 cm⁻¹ corresponded to the coordinated N-H in-plane vibration in the porphyrin ring.⁶² However, for TCPP(Fe), Co-TCPP(Fe)-Rod, and DLS-2D-Co-TCPP(Fe), the N-H in-plane vibration changed to 1004 cm⁻¹, demonstrating that hydrogen protons had been substituted by Fe³⁺. Furthermore, the two strong separated bands at 1605 and 1400 cm⁻¹ were assigned to $\nu_a(\text{COO}^-)$ and $\nu_s(\text{COO}^-)$. In addition, the C=O characteristic absorption at 1700 cm⁻¹ disappeared in Co-TCPP(Fe)-Rod and DLS-2D-Co-TCPP(Fe), jointly demonstrating that the COO⁻ group of TCPP(Fe) was bidentate and coordinated with Co²⁺ to format the structure of Co₂(COO)₄ paddlewheel unit cells. For DLS-2D-Co-TCPP(Fe)/ANS-rGO,

the disappearance of the $\nu_s(\text{COO}^-)$ stretching vibration at 1400 cm^{-1} of DLS-2D-Co-TCPP(Fe)/ANS-rGO-0.5 indicated a strong interaction between the $\text{Co}_2(\text{COO})_4$ of DLS-2D-Co-TCPP(Fe) and ANS-rGO. The strongest advantage of porous materials for most applications is their highly accessible surface areas. This is especially true for sensing applications, because it enhances the interaction with target gases.^{63,64} Brunauer–Emmett–Teller (BET) analysis was conducted to characterize the specific surface area. As depicted in Fig. S3 (ESI[†]), the specific surface areas of DLS-2D-Co-TCPP(Fe) and Co-TCPP(Fe)-Rod were calculated by nitrogen adsorption–desorption isotherms to be $57.16\text{ m}^2\text{ g}^{-1}$ and $15.90\text{ m}^2\text{ g}^{-1}$, indicating that a sheet-like morphology was beneficial to enhancing the interaction between MOFs and the target gas.

Raman spectroscopy can be employed to demonstrate the compositions and atomic structures of materials. As shown in Fig. 2(g), two remarkable peaks of rGO and ANS-rGO at about 1357 cm^{-1} and 1600 cm^{-1} could be attributed to D and G bands, respectively. For carbon-based materials, the D band is described to analyze structural defects or disorder of sp^2 carbon, whereas the G band is attributed to the E_{2g} stretching vibration of sp^2 carbon.⁶⁵ Accordingly, the peak intensity ratio of the D band and G band (I_D/I_G) is often used to characterize the degree of disorder and defect density in carbon-based materials.⁶⁶ Consequently, the I_D/I_G values of rGO and ANS-rGO were 1.217 and 1.021, respectively, confirming that ANS influenced the degree of disorder and defect density of rGO.^{67,68} Hence, there were more functional groups around the defects and edges of ANS-rGO that facilitated the assembly of ANS-rGO and MOFs through coordination interaction.^{69,70} For DLS-2D-Co-TCPP(Fe), the peak at 1554 cm^{-1} was ascribed to the C–N bond in TCPP(Fe). The peaks at 1012 cm^{-1} and 1084 cm^{-1} belonged to $\delta\text{ C}_{\text{ph}}\text{--H}$ and $\delta\text{ C}_{\beta}\text{--H}$, respectively, in the porphyrin structure.^{71,72} The characteristic peaks at 385 cm^{-1} and 1358 cm^{-1} were assigned to the Fe–N breathing mode and Fe–N bond of pyrrole deformation mode, respectively.⁷³ The peak at 392 cm^{-1} was attributed to the Co–O bond, indicating the formation of a $\text{Co}_2(\text{COO})_4$ paddlewheel structure, which was in accordance with XRD data. Additionally, the peaks of DLS-2D-Co-TCPP(Fe)/ANS-rGO presented all the typical peaks of ANS-rGO and DLS-2D-Co-TCPP(Fe).

X-ray photoelectron spectroscopy (XPS) was undertaken to elucidate the composition of elements, coordination geometries, and valence states. The XPS survey spectrum of DLS-2D-Co-TCPP(Fe) (Fig. S2a, ESI[†]) indicated that it mainly consisted of Co, Fe, O, N, and C. The XPS survey spectrum of ANS-rGO demonstrated that it mainly contained O, N, C, and S. The XPS survey spectrum of DLS-2D-Co-TCPP(Fe)/ANS-rGO-0.5 showed all the elements of DLS-2D-Co-TCPP(Fe) and ANS-rGO. The high-resolution spectra of C 1s of DLS-2D-Co-TCPP(Fe) and DLS-2D-Co-TCPP(Fe)/ANS-rGO-0.5 are shown in Fig. S2b (ESI[†]). The peaks at 284.8 eV, 286.0 eV, 288.5 eV, and 290.1 eV were associated with C–C, C–O, C–N, and C=O, respectively.⁷⁴ The high-resolution spectra of S 2p of ANS-rGO and DLS-2D-Co-TCPP(Fe)/ANS-rGO-0.5 with the same peaks at 169.6 eV and 168.2 eV were assigned to S 2p_{3/2} and S 2p_{1/2}, respectively, in Fig. S2c (ESI[†]).

The high-resolution spectra of O 1s of ANS-rGO and DLS-2D-Co-TCPP(Fe)/ANS-rGO-0.5 are shown in Fig. 2(h). For ANS-rGO, the peaks at 532.2 eV and 533.7 eV corresponded to C=O and C–OH, respectively. For DLS-2D-Co-TCPP(Fe)/ANS-rGO, the peaks at 532.0 eV, and 533.6 eV could be attributed to C=O and C–OH, respectively. As a result, the binding energy of C=O and C–OH in DLS-2D-Co-TCPP(Fe)/ANS-rGO-0.5 exhibited a slight decrease when compared with that of ANS-rGO, indicating that the electron cloud shifted from DLS-2D-Co-TCPP(Fe) to ANS-rGO. To further demonstrate carrier migration at the interface between ANS-rGO and DLS-2D-Co-TCPP(Fe), the binding energy of Co 2p, Fe 2p, and N 1s was demonstrated by XPS, respectively. The Co 2p peaks of DLS-2D-Co-TCPP(Fe) and DLS-2D-Co-TCPP(Fe)/ANS-rGO-0.5 are displayed in Fig. 2(i). For DLS-2D-Co-TCPP(Fe), 781.5 eV and 785.7 eV were assigned to a 2p_{3/2} peak and a satellite peak, respectively. Besides, 797.3 eV (2p_{1/2}) and 802.7 eV (satellite splitting) described the binding energy of Co 2p.⁷⁵ Compared with DLS-2D-Co-TCPP(Fe), the Co 2p XPS characteristic spectra of DLS-2D-Co-TCPP(Fe)/ANS-rGO-0.5 showed similar peaks at 781.8 eV (2p_{3/2}), 786.9 eV (satellite splitting), 797.7 (2p_{1/2}), and 803.3 eV (satellite splitting). The binding energy of DLS-2D-Co-TCPP(Fe)/ANS-rGO-0.5 increased by $\sim 0.3\text{ eV}$ compared with that of DLS-2D-Co-TCPP(Fe) indicating that electrons were transferred from DLS-2D-Co-TCPP(Fe) to ANS-rGO. For Fe 2p peaks, DLS-2D-Co-TCPP(Fe) displayed a 2p_{3/2} peak at 711.2 eV and a satellite peak at 716.3 eV, with their corresponding splitting peaks at 723.5 eV (2p_{1/2}) and 730.6 eV (satellite splitting), respectively, in Fig. 2(j). Compared with DLS-2D-Co-TCPP(Fe), the Fe 2p XPS characteristic spectra of DLS-2D-Co-TCPP(Fe)/ANS-rGO-0.5 at 711.5 eV (2p_{3/2}), 716.8 eV (satellite splitting), 724.1 (2p_{1/2}), and 731.0 eV (satellite splitting) were shifted positively, verifying carrier migration between ANS-rGO and Co-TCPP(Fe).⁶⁰ Fig. S2d (ESI[†]) shows the N 1s peak of DLS-2D-Co-TCPP(Fe), ANS-rGO, and DLS-2D-Co-TCPP(Fe)/ANS-rGO-0.5. For ANS-rGO, the peaks at 398.7 eV and 401.0 eV were assigned to N–C and N–H, respectively. For DLS-2D-Co-TCPP(Fe), the peaks at 398.4 eV and 399.5 eV corresponded to N–C and N–Fe, respectively. For DLS-2D-Co-TCPP(Fe)/ANS-rGO-0.5, peaks at 398.4 eV, 400.0 eV, and 401.4 eV were attributed to N–C, N–Fe, and N–H, respectively. The binding energy of N–Fe of DLS-2D-Co-TCPP(Fe)/ANS-rGO-0.5 was shifted positively compared with that of DLS-2D-Co-TCPP(Fe), which corresponded with the results of Fe 2p XPS survey spectra.

Consequently, for the DLS-2D-Co-TCPP(Fe)/ANS-rGO SOS architecture, the binding energy of O 1s around the defects and edges in ANS-rGO was shifted negatively. The binding energy of Co 2p and Fe 2p in DLS-2D-Co-TCPP(Fe) was shifted positively. As a result, there was a trend of coordination interaction between DLS-2D-Co-TCPP(Fe) and ANS-rGO to form stable hybrids.^{70,76} These characterizations confirmed that assembling ANS-rGO with DLS-2D-Co-TCPP(Fe) to construct a SOS architecture did not compromise the structural integrity of DLS-2D-Co-TCPP(Fe). Meanwhile, coordination interaction between DLS-2D-Co-TCPP(Fe) and ANS-rGO could greatly contribute to the high stability of the SOS architecture.

Measurement of NO-sensing properties

The robust electronic transmission capacity inherent in heterojunctions serves as an underpinning for the development of high-performance gas sensors.

We investigated the gas-sensing capabilities of sensors employing various materials (rGO, ANS-rGO, Co-TCPP(Fe)-Rod, DLS-2D-Co-TCPP(Fe), Co-TCPP(Fe)-Rod/ANS-rGO, and DLS-2D-Co-TCPP(Fe)/ANS-rGO) at room temperature in a nitrogen atmosphere.

Fig. 3(a) illustrates the sensing-response curves corresponding to NO (10 ppm) for rGO, ANS-rGO, Co-TCPP(Fe)-Rod, DLS-2D-Co-TCPP(Fe), Co-TCPP(Fe)-Rod/ANS-rGO, and DLS-2D-Co-TCPP(Fe)/ANS-rGO. The sensing performance of rGO and ANS-rGO towards NO was inconspicuous. Co-TCPP(Fe)-Rod and DLS-2D-Co-TCPP(Fe) did not exhibit gas responses because of the poor conductivity of pure MOF.

The response characteristic of the Co-TCPP(Fe)-Rod/ANS-rGO-based sensor was improved obviously compared with that

of the single material. The performance of the DLS-2D-Co-TCPP(Fe)/ANS-rGO-based sensor was much better than that of the other samples because Co-TCPP(Fe)-Rod had lower resistance to carrier migration than DLS-2D-Co-TCPP(Fe). Its superior gas-sensing performance emanated from the large amount of Fe-N₄, lower resistance to carrier migration of the nanosheets structure, the heterojunction between DLS-2D-Co-TCPP(Fe) and ANS-rGO, and the mass ratio of DLS-2D-Co-TCPP(Fe) to ANS-rGO. Notably, unmodified rGO served as a reference in the preparation of sensors for Co-TCPP(Fe)-Rod/rGO and DLS-2D-Co-TCPP(Fe)/rGO, underscoring the importance of ANS-rGO with the donor- π -acceptor dipole in the sensing system.

As shown in Fig. S6 (ESI[†]), an array of DLS-2D-Co-TCPP(Fe)/ANS-rGO hybrid materials with feed mass ratios of 0.05 : 1, 0.1 : 1, 0.3 : 1, 0.5 : 1, and 0.9 : 1 (DLS-2D-Co-TCPP(Fe):ANS-rGO) were obtained and named as DLS-2D-Co-TCPP(Fe)/ANS-rGO-0.05, DLS-2D-Co-TCPP(Fe)/ANS-rGO-0.1, DLS-2D-Co-TCPP(Fe)/ANS-rGO-0.3,

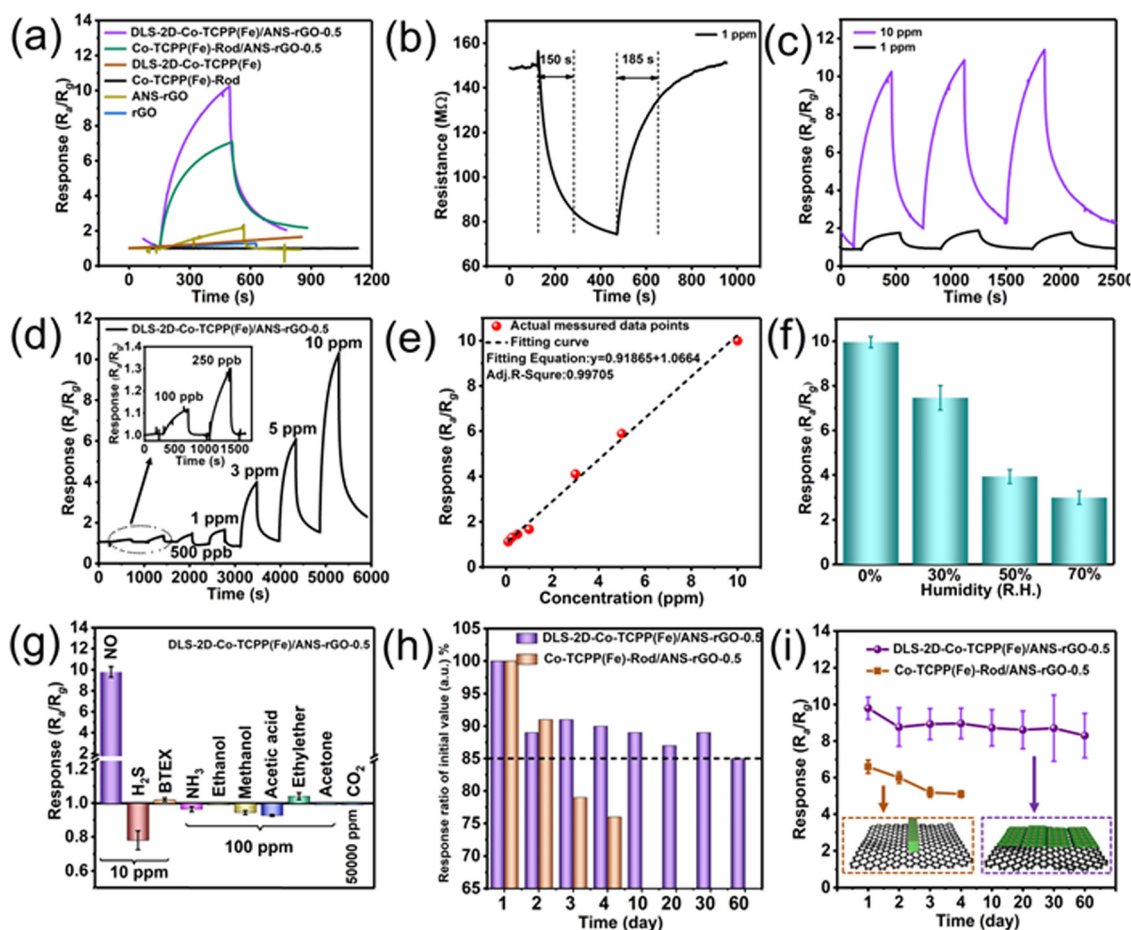


Fig. 3 (a) Typical response curves after exposure of NO (10 ppm) to pristine rGO, ANS-rGO, Co-TCPP(Fe)-Rod, DLS-2D-Co-TCPP(Fe), Co-TCPP(Fe)-Rod/ANS-rGO, and DLS-2D-Co-TCPP(Fe)/ANS-rGO. (b) Real-time response–recovery characteristics of the DLS-2D-Co-TCPP(Fe)/ANS-rGO-0.5-based sensor to NO (1 ppm) at RT. (c) Cyclic stability of the sensor to NO (1 ppm and 10 ppm) at RT. (d) Response curves of DLS-2D-Co-TCPP(Fe)/ANS-rGO-based sensors to NO (100 ppb to 10 ppm). (e) The corresponding fitted curve of the response. (f) Gas-sensing response of a DLS-2D-Co-TCPP(Fe)/ANS-rGO-0.5-based sensor towards NO (10 ppm) under different values of relative humidity at RT. (g) Selectivity of the sensor to various gases. (h) Response ratio of the initial value (a.u.) % of DLS-2D-Co-TCPP(Fe)/ANS-rGO-0.5 and Co-TCPP(Fe)-Rod/ANS-rGO-0.5. (i) Long-term stability of DLS-2D-Co-TCPP(Fe)/ANS-rGO-0.5 and Co-TCPP(Fe)-Rod/ANS-rGO-0.5 exposed to NO (10 ppm) at RT.

DLS-2D-Co-TCPP(Fe)/ANS-rGO-0.5, and DLS-2D-Co-TCPP(Fe)/ANS-rGO-0.9, respectively. Among them, the DLS-2D-Co-TCPP(Fe)/ANS-rGO-0.5-based sensor demonstrated superior sensitivity to NO (10 ppm) at room temperature, indicating that the mass ratio of MOF and graphene was an unignorable factor for NO sensing. As depicted in Fig. 3(b), during NO sensing, a decrease in resistance of DLS-2D-Co-TCPP(Fe)/ANS-rGO-0.5 indicated p-type semiconductor-like properties, corroborated by UPS spectra and UV-vis spectra in subsequent analyses. In addition, the sensor based on DLS-2D-Co-TCPP(Fe)/ANS-rGO-0.5 exhibited a rapid response and recovery speeds (150 s/185 s) toward NO (1 ppm) at room temperature. Importantly, the heterojunction between DLS-2D-Co-TCPP(Fe) and ANS-rGO facilitated carrier migration, contributing to the preparation of high-performance NO sensors. Moreover, Fig. 3(c) demonstrates the superior repeatability of the DLS-2D-Co-TCPP(Fe)/ANS-rGO-0.5-based sensor towards NO (1 ppm and 10 ppm).

Fig. 3(d) displays the successive sensing response–recovery curves of the DLS-2D-Co-TCPP(Fe)/ANS-rGO-0.5-based sensor toward NO (0.1–10 ppm) with the corresponding response values (R_a/R_g) from 1.12 to 10.11. The pLOD of the DLS-2D-Co-TCPP(Fe)/ANS-rGO-0.5-based sensor was as low as 100 ppb, indicating that it could be employed for practical applications. As shown in Fig. 3(e), the response values of the DLS-2D-Co-TCPP(Fe)/ANS-rGO-0.5-based sensor demonstrated a good linear relationship to the NO concentration (0.1–10 ppm), which is important for practical applications. The sensors operable at room temperature were intended to be developed, so the effect of relative humidity was tested (Fig. 3(f) and Fig. S3, ESI†). The response of DLS-2D-Co-TCPP(Fe)/ANS-rGO-0.5 towards NO (10 ppm) was measured in dry N_2 , 30% relative humidity (R.H.) N_2 , 50% R.H. N_2 , and 70% R.H. N_2 , respectively. The sensor displayed diminishing response as R.H. increased, which was attributed to the competition between water molecules and NO molecules adsorbed on the surface of sensors. As illustrated in Fig. 3(g), the DLS-2D-Co-TCPP(Fe)/ANS-rGO-0.5-based sensor demonstrated significantly heightened responsiveness to NO ($R_a/R_g = 10.11$, 10 ppm) than other exhaled gases, including H_2S ($R_a/R_g = 0.78$, 10 ppm), BTEX (benzene, toluene, ethylbenzene, *o*-Xylene; $R_a/R_g = 1.02$,

10 ppm), ammonia ($R_a/R_g = 0.96$, 100 ppm), ethanol ($R_a/R_g = 1.01$, 100 ppm), methanol ($R_a/R_g = 0.94$, 100 ppm), acetic acid ($R_a/R_g = 0.92$, 100 ppm), ethylether ($R_a/R_g = 1.04$, 100 ppm), acetone ($R_a/R_g = 0.99$, 100 ppm), and CO_2 ($R_a/R_g = 1.01$, 50 000 ppm). The higher selectivity of the sensor towards NO could be attributed to the abundant Fe- N_4 active units in DLS-2D-Co-TCPP(Fe), which provided plentiful specific chemisorbed sites for NO sensing. The selectivity for this composite towards NO could be improved further by controlling the morphology of MOFs to enhance the porosity and specific surface area to promote interactions between Fe- N_4 active units in the center of the porphyrin derivatives of MOFs and NO.^{77–79}

For the clinical diagnosis of gas sensors, it is imperative to consider the impact of humidity on the sensing process. The long-term stability of the sensor can be verified by an aging test.^{80–82} As displayed in Fig. 3(h)–(i), the response of the DLS-2D-Co-TCPP(Fe)/ANS-rGO-0.5-based sensor remained at ~85% of the initial response over 60 days, indicating that the sensor has good repeatability and recoverability. The DLS-2D-Co-TCPP(Fe)/ANS-rGO-0.5-based sensor displayed higher sensitivity along with higher stability than Co-TCPP(Fe)-Rod/ANS-rGO-0.5 towards NO. This observation suggests that the SOS architectural heterojunction served as an effective strategy for consistently enhancing the performance of sensing materials.

That is, the coordination interaction in the SOS architectural heterojunction provided a highly coupled interface that improved the stability as well as facilitated carrier migration of the hybrid, which has enormous potential for sensing applications. In Table 1, for comparison, the excellent performance of the DLS-2D-Co-TCPP(Fe)/ANS-rGO-0.5-based sensor was competitive with the existing typical chemiresistive NO sensors based on MOFs reported so far at room temperature.

Formation mechanism of SOS architectural heterojunctions

Owing to the favorable electrical conductivity of ANS-rGO promoting the carrier migration of the DLS-2D-Co-TCPP(Fe)/ANS-rGO-0.5 SOS architecture, the sensing mechanism of the DLS-2D-Co-TCPP(Fe)/ANS-rGO-0.5-based sensor towards NO could be interpreted by the heterojunction theory. Ultra-violet photoelectron spectroscopy (UPS), UV-Vis, and XPS were

Table 1 Performance comparison of MOF-based chemiresistive NO sensors at room temperature

Materials	NO (ppm)	Response ^a	T_{res}/T_{rec} ^b (s/s)	pLOD ^c (ppm)	Stability ^d (days)
Ni ₃ HITP ₂ ⁸³	5	~1.38	3600/—	5	<50
Ni ₃ HHTP ₂ ⁸³	5	~1.19	3600/—	5	<50
NiPc-Ni ⁴⁹	1	~1.37	90/—	0.02	—
NiPc-Cu ⁴⁹	1	~1.45	90/—	0.02	—
Ni ₃ HHTP ₂ ²²	10	~1.42	300/—	2.5	—
Cu ₃ HHTP ₂ ²²	10	~1.18	300/—	2.5	—
Cu-TCA/TiNC ⁸⁴	1	~1.2	35/110 (under UV light)	0.2	30
Co-TCPP(Fe)/Ti ₃ C ₂ T _x -20 ³¹	5	1.55	95/15	0.2	10
rGO/PDDA/Co ₃ (HITP) ₂ ³⁵	1	1.13	100/50	0.1	~4
DLS-2D-Co-TCPP(Fe)/ANS-rGO-0.5	1	1.82	150/185	0.1	>60
(This work)	0.25	1.33			

^a Response = R_a/R_g . (R_a represents the resistance captured in N_2 and R_g represents the resistance captured in the target gas). ^b T_{res} and T_{rec} represent response time and recovery time. ^c pLOD represents practical LOD. ^d The 85% response of the initial value is set the boundary value of stability.

undertaken to expound the sensing mechanism collectively. To illustrate carrier migration in the heterojunction, UPS was displayed to explore the work functions of ANS-rGO, DLS-2D-Co-TCPP(Fe), and DLS-2D-Co-TCPP(Fe)/ANS-rGO (Fig. 4(a)), which were determined from the intercepts of the two tangents on the x-axis named $E_{\text{cut-off-1}}$ and $E_{\text{cut-off-2}}$ (Fig. 4(b) and (c)). The work functions (W_f) calculated by eqn (1) at 4.49 eV and 3.91 eV were assigned to ANS-rGO and DLS-2D-Co-TCPP(Fe) in the heterojunction, respectively, for which electrons moved from DLS-2D-Co-TCPP(Fe) to ANS-rGO.

$$W_f = -(h\nu - E_{\text{cut-off-2}}) = -(21.2 - E_{\text{cut-off-2}}) \quad (1)$$

Bandgaps of DLS-2D-Co-TCPP(Fe) and DLS-2D-Co-TCPP(Fe)/ANS-rGO calculated using eqn (2) were demonstrated by UV-Vis spectra.

$$(\alpha h\nu)^2 = A (h\nu - E_g) \quad (2)$$

where E_g was the bandgap of DLS-2D-Co-TCPP(Fe) and DLS-2D-Co-TCPP(Fe)/ANS-rGO, α was the absorption coefficient, $h\nu$ was the photon energy, and A was a constant.

The UV-vis spectra of DLS-2D-Co-TCPP(Fe), ANS-rGO, and DLS-2D-Co-TCPP(Fe)/ANS-rGO-0.5 are displayed in Fig. 4(d). The bandgaps of DLS-2D-Co-TCPP(Fe) and DLS-2D-Co-TCPP(Fe)/ANS-rGO-0.5 were 2.50 eV and 2.45 eV, respectively, as calculated by the Tauc plots in Fig. 4(e). The bandgap of a semiconductor is an important factor impacting carrier migration during gas sensing. Notably, the bandgap of DLS-2D-Co-TCPP(Fe)/ANS-rGO was smaller than that of DLS-2D-Co-TCPP(Fe), which reduced the difficulty of carrier migration in NO sensing.³¹

As displayed in Fig. 4(g), the highest occupied molecular orbital (HOMO) and lowest unoccupied molecular orbital (LUMO) calculated by eqn (3) and (4) jointly illustrated the bandgap of DLS-2D-Co-TCPP(Fe) and DLS-2D-Co-TCPP(Fe)/ANS-rGO-0.5. The Fermi level (E_f) of DLS-2D-Co-TCPP(Fe) was close to LUMO, illustrating that DLS-2D-Co-TCPP(Fe) was an

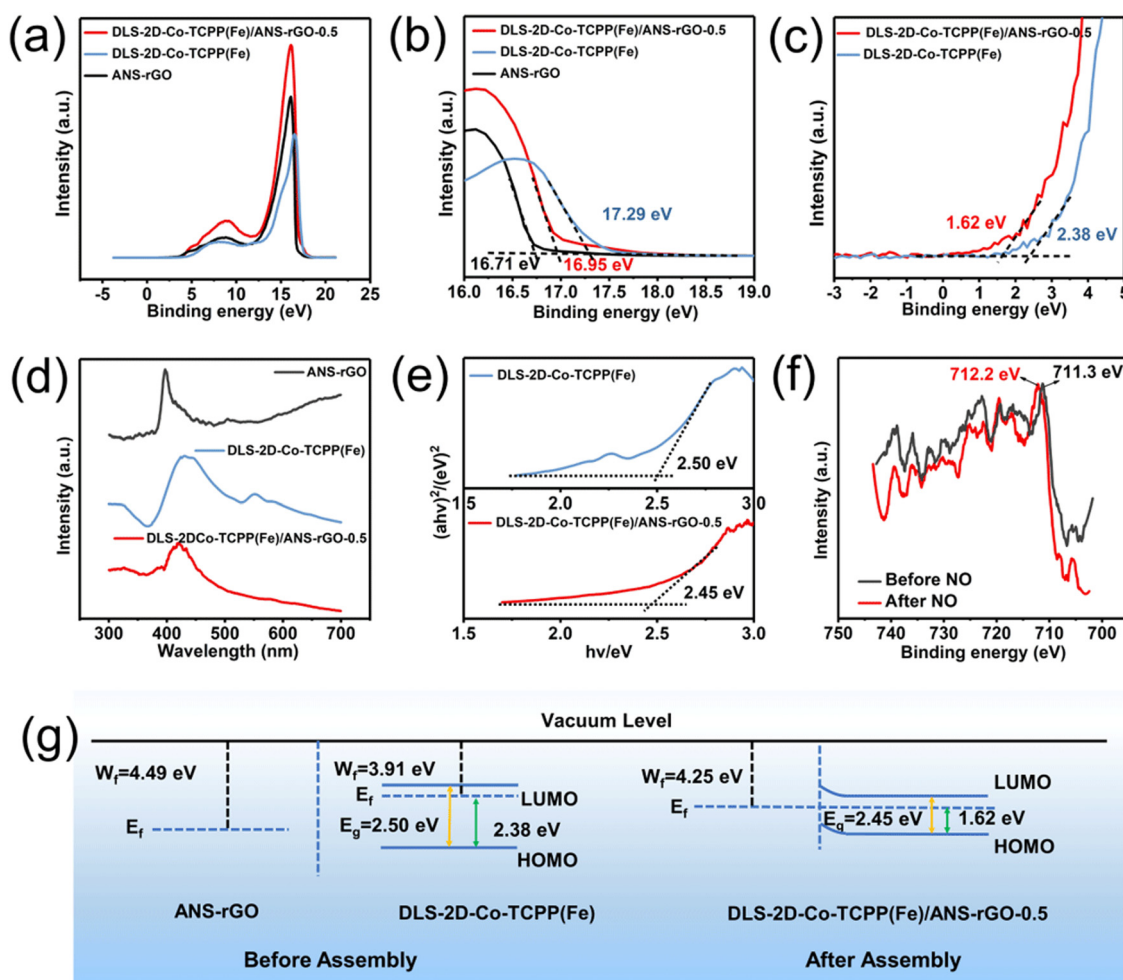


Fig. 4 (a)–(c) UPS spectra of ANS-rGO, DLS-2D-Co-TCPP(Fe), and DLS-2D-Co-TCPP(Fe)/ANS-rGO-0.5. (d) UV-vis spectra of DLS-2D-Co-TCPP(Fe), ANS-rGO, and DLS-2D-Co-TCPP(Fe)/ANS-rGO-0.5. (e) Tauc plots of DLS-2D-Co-TCPP(Fe) and DLS-2D-Co-TCPP(Fe)/ANS-rGO-0.5. (f) High-resolution XPS spectra of Fe 2p for DLS-2D-Co-TCPP(Fe)/ANS-rGO-0.5 before and after exposure to NO. (g) Energy scheme before and after assembly between ANS-rGO and DLS-2D-Co-TCPP(Fe).

n-type like semiconductor. Meanwhile, the E_f of DLS-2D-Co-TCPP(Fe)/ANS-rGO-0.5 remained close to LUMO, illustrating that DLS-2D-Co-TCPP(Fe)/ANS-rGO-0.5 was also an n-type-like semiconductor.

$$\text{HOMO} = W_f - E_{\text{cut-off-1}} \quad (3)$$

$$\text{LUMO} = \text{HOMO} + E_g \quad (4)$$

The E_f of ANS-rGO was lower than that of DLS-2D-Co-TCPP(Fe), indicating that electrons migrated from DLS-2D-Co-TCPP(Fe) to ANS-rGO at the interfaces of heterojunctions.

Proposed mechanism of NO sensing

We wished to further confirm carrier migration between the DLS-2D-Co-TCPP(Fe)/ANS-rGO-0.5 SOS architectural heterojunction and NO. XPS was carried out to explain the change in surface electronic states of DLS-2D-Co-TCPP(Fe)/ANS-rGO-0.5 SOS architectural heterojunctions before and after exposure to NO at room temperature.

For the spectra of Fe 2p (Fig. 4(f)), the peaks of Fe 2p were shifted positively, indicating that electrons were transferred from the DLS-2D-Co-TCPP(Fe)/ANS-rGO-0.5 SOS architectural heterojunction to gas molecules during sensing.⁸⁵

The sensing mechanism of a sensor is depicted in Fig. 5. Owing to the built-in electric field in the DLS-2D-Co-TCPP(Fe)/ANS-rGO SOS architectural heterojunction, electrons were transferred from DLS-2D-Co-TCPP(Fe) to ANS-rGO and holes

were transferred from ANS-rGO to DLS-2D-Co-TCPP(Fe) on the interface of the heterojunction, which led to the separation of carriers and formation of a depletion layer. The concentration of electrons decreased and the depletion layer widened because NO had electron affinity and can capture electrons readily from the conduction band of the heterojunction. As a result, the resistance of the heterojunction decreased dramatically upon NO exposure.

Conclusions

We designed a chemiresistive NO sensor based on Co-TCPP(Fe)/ANS-rGO with a SOS architectural heterojunction, which showed high sensitivity and long-term stability. First, a novel porphyrin-based MOF DLS-2D-Co-TCPP(Fe) with high dispersion, large size, and sheet-like morphology was prepared by liquid-phase exfoliation. The obtained DLS-2D-Co-TCPP(Fe) was assembled with ANS-rGO to form a heterojunction (DLS-2D-Co-TCPP(Fe)/ANS-rGO) with a SOS architectural heterojunction through coordination interaction. Second, the DLS-2D-Co-TCPP(Fe)/ANS-rGO-based sensor demonstrated excellent NO-sensing performance ($R_a/R_g = 1.33$, 250 ppb) with a pLOD of 100 ppb and reliable repeatability at room temperature. Moreover, the sensor showed superior selectivity against other exhaled gases. Third, the SOS architecture had a crucial role in formation of a stable heterojunction, which was beneficial for high-sensitivity and high-stability NO sensing. This work demonstrates a convenient strategy of building a stable heterojunction between graphene and MOF for high-performance chemiresistive gas sensors. This strategy could be employed to fabricate MOF-based hybrid sensing materials in the future.

Author contributions

Y.-W. C. and Y. W. conceived and designed the research. Y.-W. C. carried out experiments. J.-X. Z. and R.-F. L. simulated the model of MOF. W.-R. L. and Y.-C. F. assisted in material preparation. Y.-X. G., H.-H. Y., F.-N. W., and H. L. helped to conduct data analyses. Y.-K. L. P.-J. F., A.-M. U. S., and G.-F. Z. helped to revise the manuscript. Y.-W. C. and Y. W. wrote the manuscript with inputs from all authors. All authors discussed, revised, and approved the final version of the manuscript.

Conflicts of interest

There are no conflicts of interest to declare.

Acknowledgements

This work was supported by the National Natural Science Foundation of China (51973070), Science and Technology Program of Guangzhou (2019050001), Guangdong Basic and Applied Basic Research Foundation (2022A1515010577, 2021A1515012420), Innovative Team Project of Education Bureau of Guangdong Province (2018KCXTD009), Guangdong

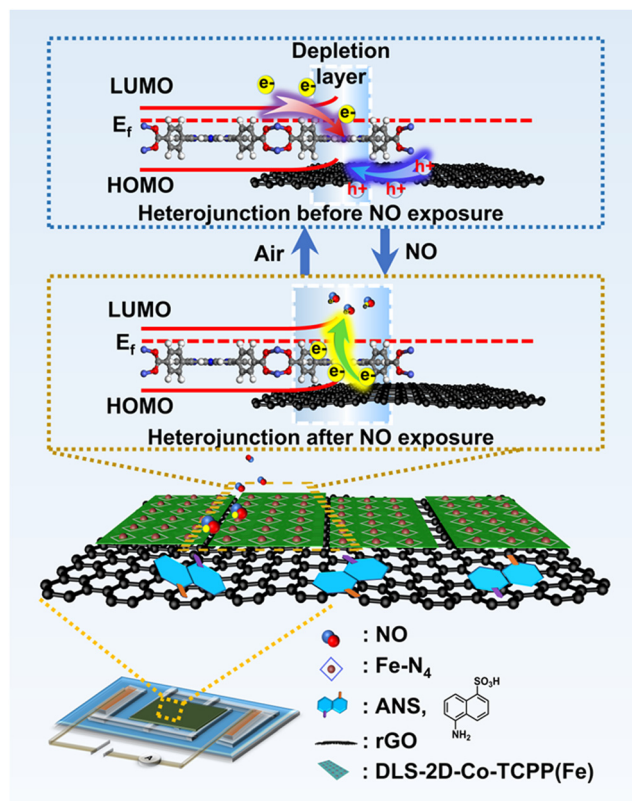


Fig. 5 Proposed sensing mechanism of DLS-2D-Co-TCPP(Fe)/ANS-rGO towards NO (schematic).

Science and Technology Project-International Cooperation (2022A0505050069), Startup Foundation from SCNU, Guangdong Provincial Key Laboratory of Optical Information Materials and Technology (2023B1212060065), MOE International Laboratory for Optical Information Technologies, the 111 Project, and High-end Foreign Experts Recruitment Program (DL2023030001L). Calculations were made at Bianshui Riverside Supercomputing Center (BRSC).

Notes and references

- M. D. Brown and M. H. Schoenfish, *Chem. Rev.*, 2019, **119**, 11551–11575.
- V. Calabrese, C. Mancuso, M. Calvani, E. Rizzarelli, D. A. Butterfield and A. M. Giuffrida Stella, *Nat. Rev. Neurosci.*, 2007, **8**, 766–775.
- L. E. Gustafsson, A. Leone, M. Persson, N. Wiklund and S. Moncada, *Biochem. Biophys. Res. Commun.*, 1991, **181**, 852–857.
- C. Li, B.-Y. Song, M.-S. Lv, G.-L. Chen, X.-F. Zhang, Z.-P. Deng, Y.-M. Xu, L.-H. Huo and S. Gao, *Chem. Eng. J.*, 2022, **446**, 136846.
- B.-Y. Song, C. Li, X.-F. Zhang, R. Gao, X.-L. Cheng, Z.-P. Deng, Y.-M. Xu, L.-H. Huo and S. Gao, *J. Mater. Chem. A*, 2022, **10**, 14411–14422.
- N. Chakraborty and S. Mondal, *Mater. Horiz.*, 2022, **9**, 1750–1762.
- Y. Yong, X. Su, Q. Zhou, Y. Kuang and X. Li, *Sci. Rep.*, 2017, **7**, 1–12.
- Y. Wang, S. Zhang, D. Xiao, S. Wang, T. Zhang, X. Yang, S. Heng and M. Sun, *Sens. Actuators, B*, 2023, **374**, 132823.
- B. Zhang, J.-Y. Sun and P.-X. Gao, *ACS Sens.*, 2021, **6**, 2979–2987.
- Y. Hu, X. Hu, J. Qiu, W. Quan, W. Qin, X. Min, S. Lu, S. Chen, W. Du and X. Chen, *ACS Appl. Mater. Interfaces*, 2018, **10**, 42583–42592.
- Y. Xu, W. Zheng, X. Liu, L. Zhang, L. Zheng, C. Yang, N. Pinna and J. Zhang, *Mater. Horiz.*, 2020, **7**, 1519–1527.
- N. Tammanoon, T. Iwamoto, T. Ueda, T. Hyodo, A. Wisitsoraat, C. Liewhiran and Y. Shimizu, *ACS Appl. Mater. Interfaces*, 2020, **12**, 41728–41739.
- Y. Liu, Y. Jiao, Z. Zhang, F. Qu, A. Umar and X. Wu, *ACS Appl. Mater. Interfaces*, 2014, **6**, 2174–2184.
- S. S. Shendage, V. L. Patil, S. A. Vanalakar, S. P. Patil, N. S. Harale, J. L. Bhosale, J. H. Kim and P. S. Patil, *Sens. Actuators, B*, 2017, **240**, 426–433.
- H. G. Moon, Y. Jung, S. D. Han, Y.-S. Shim, W.-S. Jung, T. Lee, S. Lee, J. H. Park, S.-H. Baek, J.-S. Kim, H.-H. Park, C. Kim and C.-Y. Kang, *Sens. Actuators, B*, 2018, **257**, 295–302.
- Z. Li, H. Li, Z. Wu, M. Wang, J. Luo, H. Torun, P. Hu, C. Yang, M. Grundmann, X. Liu and Y. Fu, *Mater. Horiz.*, 2019, **6**, 470–506.
- I.-D. Kim, A. Rothschild and H. L. Tuller, *Acta Mater.*, 2013, **61**, 974–1000.
- C. Balamurugan, S. J. Song and D. W. Lee, *Sens. Actuators, B*, 2018, **272**, 400–414.
- H.-Y. Li, S.-N. Zhao, S.-Q. Zang and J. Li, *Chem. Soc. Rev.*, 2020, **49**, 6364–6401.
- W.-T. Koo, J.-S. Jang and I.-D. Kim, *Chem*, 2019, **5**, 1938–1963.
- J. F. Olorunyomi, S. T. Geh, R. A. Caruso and C. M. Doherty, *Mater. Horiz.*, 2021, **8**, 2387–2419.
- M. K. Smith, K. E. Jensen, P. A. Pivak and K. A. Mirica, *Chem. Mater.*, 2016, **28**, 5264–5268.
- M.-S. Yao, X.-J. Lv, Z.-H. Fu, W.-H. Li, W.-H. Deng, G.-D. Wu and G. Xu, *Angew. Chem., Int. Ed.*, 2017, **56**, 16510–16514.
- M. G. Campbell, S. F. Liu, T. M. Swager and M. Dinca, *J. Am. Chem. Soc.*, 2015, **137**, 13780–13783.
- M. K. Smith, K. E. Jensen, P. A. Pivak and K. A. Mirica, *Chem. Mater.*, 2016, **28**, 5264–5268.
- A. Aykanat, C. G. Jones, E. Cline, R. M. Stolz, Z. Meng, H. M. Nelson and K. A. Mirica, *ACS Appl. Mater. Interfaces*, 2021, **13**, 60306–60318.
- K. S. Novoselov, A. Mishchenko, A. Carvalho and A. H. Castro Neto, *Science*, 2016, **353**, aac9439.
- S. Aftab, M. Z. Iqbal, S. Hussain, H. H. Hegazy, F. Kabir, S. H. A. Jaffery and G. Koyyada, *Chem. Eng. J.*, 2023, **469**, 144039.
- M.-S. Yao, J.-W. Xiu, Q.-Q. Huang, W.-H. Li, W.-W. Wu, A.-Q. Wu, L.-A. Cao, W.-H. Deng, G.-E. Wang and G. Xu, *Angew. Chem., Int. Ed.*, 2019, **58**, 14915–14919.
- A.-M. Andringa, M.-J. Spijkman, E. C. Smits, S. G. Mathijssen, P. A. Van Hal, S. Setayesh, N. P. Willard, O. V. Borshchev, S. A. Ponomarenko and P. W. Blom, *Org. Electron.*, 2010, **11**, 895–898.
- Y. Chang, M. Chen, Z. Fu, R. Lu, Y. Gao, F. Chen, H. Li, N. F. De Rooij, Y.-K. Lee, Y. Wang and G. Zhou, *J. Mater. Chem. A*, 2023, **11**, 6966–6977.
- F. M. A. Noa, M. Abrahamsson, E. Ahlberg, O. Cheung, C. R. Gob, C. J. McKenzie and L. Ohlstrom, *Chem*, 2021, **7**, 2491–2512.
- H. Gu, G. Shi, L. Zhong, L. Liu, H. Zhang, C. Yang, K. Yu, C. Zhu, J. Li, S. Zhang, C. Chen, Y. Han, S. Li and L. Zhang, *J. Am. Chem. Soc.*, 2022, **144**, 21502–21511.
- Z. Xu, K. Wu, S. Zhang, Y. Meng, H. Li and L. Li, *Mater. Horiz.*, 2017, **4**, 383–388.
- S. Xu, X. Liu, J. Wu and J. Wu, *ACS Sens.*, 2023, **8**, 2348–2358.
- C. Lamiel, I. Hussain, O. R. Ogunsakin and K. Zhang, *J. Mater. Chem. A*, 2022, **10**, 14247–14272.
- H.-W. Guo, Z. Hu, Z.-B. Liu and J.-G. Tian, *Adv. Funct. Mater.*, 2021, **31**, 2007810.
- M. Zhao, Y. Wang, Q. Ma, Y. Huang, X. Zhang, J. Ping, Z. Zhang, Q. Lu, Y. Yu and H. Xu, *Adv. Mater.*, 2015, **27**, 7372–7378.
- M. Xu, D. Li, K. Sun, L. Jiao, C. Xie, C. Ding and H.-L. Jiang, *Angew. Chem., Int. Ed.*, 2021, **60**, 16372–16376.
- A. Gallego, C. Hermosa, O. Castillo, I. Berlanga, C. J. Gomez-Garcia, E. Mateo-Marti, J. I. Martinez, F. Flores, C. Gomez-Navarro, J. Gomez-Herrero, S. Delgado and F. Zamora, *Adv. Mater.*, 2013, **25**, 2141–2146.

- 41 W. Pei, T. Zhang, Y. Wang, Z. Chen, A. Umar, H. Li and W. Guo, *Nanoscale*, 2017, **9**, 16273–16280.
- 42 Y. Wang, M. Zhao, J. Ping, B. Chen, X. Cao, Y. Huang, C. Tan, Q. Ma, S. Wu and Y. Yu, *Adv. Mater.*, 2016, **28**, 4149–4155.
- 43 E.-Y. Choi, C. A. Wray, C. Hu and W. Choe, *CrystEngComm*, 2009, **11**, 553–555.
- 44 J. Jing, J. Yang, Z. Zhang and Y. Zhu, *Adv. Energy Mater.*, 2021, **11**, 2101392.
- 45 J. Wang, X. Zhang, Y. Liu, Z. Wang, P. Wang, Z. Zheng, H. Cheng, Y. Dai and B. Huang, *J. Colloid Interface Sci.*, 2021, **602**, 300–306.
- 46 S. Rayati, D. Moradi and F. Nejabat, *New J. Chem.*, 2020, **44**, 19385–19392.
- 47 Y. Zhao, J. Wang and R. Pei, *J. Am. Chem. Soc.*, 2020, **142**, 10331–10336.
- 48 D. Klyamer, R. Shutilov and T. Basova, *Sensors*, 2022, **22**, 895.
- 49 Z. Meng, A. Aykanat and K. A. Mirica, *J. Am. Chem. Soc.*, 2018, **141**, 2046–2053.
- 50 Y. Gao, J. Wang, Y. Feng, N. Cao, H. Li, N. F. De Rooij, A. Umar, P. J. French, Y. Wang and G. Zhou, *Small*, 2022, **18**, 2103259.
- 51 H. Cheng, Y. Liu, Y. Hu, Y. Ding, S. Lin, W. Cao, Q. Wang, J. Wu, F. Muhammad, X. Zhao, X. Zhao, D. Zhao, Z. Li, H. Xing and H. Wei, *Anal. Chem.*, 2017, **89**, 11552–11559.
- 52 N. Stock and S. Biswas, *Chem. Rev.*, 2012, **112**, 933–969.
- 53 O. K. Farha and J. T. Hupp, *Acc. Chem. Res.*, 2010, **43**, 1166–1175.
- 54 J. W. Wang, K. X. Wang and Y. X. Xu, *ACS Nano*, 2021, **15**, 19026–19053.
- 55 Q. K. Wang, J. Sun and D. C. Wei, *Chin. J. Chem.*, 2022, **40**, 1359–1385.
- 56 J. Wang, N. Li, Y. X. Xu and H. Pang, *Chem. – Eur. J.*, 2020, **26**, 6402–6422.
- 57 J. Yin, J. Jin, H. H. Lin, Z. Y. Yin, J. Y. Li, M. Lu, L. C. Guo, P. X. Xi, Y. Tang and C. H. Yan, *Adv. Sci.*, 2020, **7**, 1903070.
- 58 S. Witomska, T. Leydecker, A. Ciesielski and P. Samori, *Adv. Funct. Mater.*, 2019, **29**, 1901126.
- 59 H. Sun, J. Dan, Y. Liang, M. Li, J. Zhuo, Y. Kang, Z. Su, Q. Zhang, J. Wang and W. Zhang, *Nanoscale*, 2022, **14**, 11693–11702.
- 60 H. Cheng, J. Wang, Y. Yang, H. Shi, J. Shi, X. Jiao, P. Han, X. Yao, W. Chen and X. Wei, *Small*, 2022, 2200857.
- 61 Y. Chen, D. Yang, X. Xin, Z. S. Yang, Y. C. Gao, Y. H. Shi, Z. F. Zhao, K. An, W. Z. Wang, J. D. Tan and Z. T. Jiang, *J. Mater. Chem. A*, 2022, **10**, 9717–9725.
- 62 J. Mishra, D. S. Pattanayak, A. A. Das, D. K. Mishra, D. Rath and N. K. Sahoo, *J. Mol. Liq.*, 2019, **287**, 110821.
- 63 D. J. Wales, J. Grand, V. P. Ting, R. D. Burke, K. J. Edler, C. R. Bowen, S. Mintova and A. D. Burrows, *Chem. Soc. Rev.*, 2015, **44**, 4290–4321.
- 64 X. Y. Wang, Y. H. Hu and H. Wei, *Inorg. Chem. Front.*, 2016, **3**, 41–60.
- 65 H. Huang, Z. Yue, G. Li, X. Wang, J. Huang, Y. Du and P. Yang, *J. Mater. Chem. A*, 2014, **2**, 20118–20125.
- 66 J. Liu, S. Li, B. Zhang, Y. Wang, Y. Gao, X. Liang, Y. Wang and G. Lu, *J. Colloid Interface Sci.*, 2017, **504**, 206–213.
- 67 H. Liang, L. Guo, N. Cao, H. Hu, H. Li, N. Frans De Rooij, A. Umar, H. Algarni, Y. Wang and G. Zhou, *J. Mater. Chem. A*, 2021, **9**, 23955–23967.
- 68 M. A. Pimenta, G. Dresselhaus, M. S. Dresselhaus, L. G. Cancado, A. Jorio and R. Saito, *Phys. Chem. Chem. Phys.*, 2007, **9**, 1276–1291.
- 69 D. R. Dreyer, S. Park, C. W. Bielawski and R. S. Ruoff, *Chem. Soc. Rev.*, 2010, **39**, 228–240.
- 70 W. Li, Y. Zhang, P. Su, Z. Xu, G. Zhang, C. Shen and Q. Meng, *J. Mater. Chem. A*, 2016, **4**, 18747–18752.
- 71 L. Debbichi, M. C. M. De Lucas, J. F. Pierson and P. Krueger, *J. Phys. Chem. C*, 2012, **116**, 10232–10237.
- 72 J. M. Burke, J. R. Kincaid, S. Peters, R. R. Gagne, J. P. Collman and T. G. Spiro, *J. Am. Chem. Soc.*, 1978, **100**, 6083–6088.
- 73 M. R. R. Smith, C. B. B. Martin, S. Arumuganainar, A. Gilman, B. E. E. Koel and M. L. L. Sarazen, *Angew. Chem., Int. Ed.*, 2023, **135**, e202218208.
- 74 B. Zhang, P. W. Wong and A. K. An, *Chem. Eng. J.*, 2022, **430**, 133054.
- 75 Y.-X. Du, L. Liu, Y.-K. Li, R. Liu, W.-T. Lu, J.-X. Wang, G. Zhang and F.-F. Cao, *New J. Chem.*, 2022, **46**, 8271–8276.
- 76 C. Liu, J. Hou, J. Yang, M. Fang, Z. Tang, L. Li and H. G. Alemayehu, *J. Membr. Sci.*, 2022, **652**, 120479.
- 77 J. Hwang, A. Ejsmont, R. Freund, J. Goscianska, B. Schmidt and S. Wuttke, *Chem. Soc. Rev.*, 2020, **49**, 3348–3422.
- 78 N. Sikdar, M. Bhogra, U. V. Waghmare and T. K. Maji, *J. Mater. Chem. A*, 2017, **5**, 20959–20968.
- 79 B. J. Wang, S. Y. Ma, S. T. Pei, X. L. Xu, P. F. Cao, J. L. Zhang, R. Zhang, X. H. Xu and T. Han, *Sens. Actuators, B*, 2020, **321**, 128560.
- 80 W. J. Quan, J. Shi, H. Y. Luo, C. Fan, W. Lv, X. W. Chen, M. Zeng, J. H. Yang, N. T. Hu, Y. J. Su, H. Wei and Z. Yang, *ACS Sens.*, 2023, **8**, 103–113.
- 81 X. W. Chen, J. Shi, T. Wang, S. Y. Zheng, W. Lv, X. Y. Chen, J. H. Yang, M. Zeng, N. T. Hu, Y. J. Su, H. Wei, Z. H. Zhou and Z. Yang, *ACS Sens.*, 2022, **7**, 816–826.
- 82 X. W. Chen, T. Wang, J. Shi, W. Lv, Y. T. Han, M. Zeng, J. H. Yang, N. T. Hu, Y. J. Su, H. Wei, Z. H. Zhou, Z. Yang and Y. F. Zhang, *Nano-Micro Lett.*, 2022, **14**, 8.
- 83 M. K. Smith and K. A. Mirica, *J. Am. Chem. Soc.*, 2017, **139**, 16759–16767.
- 84 H. He, J. Guo, J. Zhao, J. Xu, C. Zhao, Z. Gao and Y.-Y. Song, *ACS Sens.*, 2022, **7**, 2750–2758.
- 85 Y. Niu, J. Zeng, X. Liu, J. Li, Q. Wang, H. Li, N. F. D. Rooij, Y. Wang and G. Zhou, *Adv. Sci.*, 2021, **8**, 2100472.